Astroparticle Physics 116 (2020) 102386

Contents lists available at ScienceDirect

Astroparticle Physics

journal homepage: www.elsevier.com/locate/astropartphys

The advanced Virgo longitudinal control system for the O2 observing run

F. Acernese[bp,aa], M. Agathos[bb], L. Aiello[n,y], A. Allocca[bj,ae], M.A. Aloy[by], A. Amato[ao], S. Antier[b], M. Arène[b], N. Arnaud[al,k], S. Ascenzi[n,ag], P. Astone[af], F. Aubin[am], S. Babak[b], P. Bacon[b], F. Badaracco[n,y], M.K.M. Bader[ar], J. Baird[b], F. Baldaccini[bi,ad], G. Ballardin[k], C. Barbieri[be,z], F. Barone[bs,aa], M. Barsuglia[b], D. Barta[au], A. Basti[bj,ae], M. Bawaj[ay,ad], M. Bazzan[bg,ab], M. Bejger[b,e], I. Belahcene[al], S. Bernuzzi[bb], D. Bersanetti[x,**], A. Bertolini[ar], M. Bischi[bx,w], M. Bitossi[k,ae], M.A. Bizouard[c], S. Bloemen[at], F. Bobba[bq,ai], M. Boer[c], G. Bogaert[c], F. Bondu[bl], R. Bonnand[am], B.A. Boom[ar], V. Boschi[ae], Y. Bouffanais[bg,ab], A. Bozzi[k], C. Bradaschia[ae], M. Branchesi[n,y], M. Breschi[bb], T. Briant[an], F. Brighenti[bx,w], A. Brillet[c], J. Brooks[k], T. Bulik[d], H.J. Bulten[aw,ar], D. Buskulic[am], C. Buy[b], G. Cagnoli[q], E. Calloni[bf,aa], M. Canepa[az,x], G. Carapella[bq,ai], F. Carbognani[k], G. Carullo[bj,ae], J. Casanueva Diaz[ae,*], C. Casentini[bn,ag], S. Caudill[ar], F. Cavalier[al], R. Cavalieri[k], G. Cella[ae], P. Cerdá-Durán[by], E. Cesarini[g,ag], O. Chaibi[c], E. Chassande-Mottin[b], A. Chincarini[br,ai], A. Chiummo[k], N. Christensen[c], S. Chua[an], G. Ciani[bg,ab], M. Cieślar[e], R. Ciolfi[v,ab], F. Cipriano[c], A. Cirone[az,x], F. Cleva[c], E. Coccia[n,y], P.-F. Cohadon[an], D. Cohen[al], M. Colpi[be,z], L. Conti[ab], I. Cordero-Carrión[bz], S. Corezzi[bi,ad], D. Corre[al], S. Cortese[k], J.-P. Coulon[c], M. Croquette[an], E. Cuoco[k], B. DÁngelo[az,x], S. D'Antonio[ag], V. Dattilo[k], M. Davier[al], J. Degallaix[ao], M. De Laurentis[bf,aa], S. Deléglise[an], W. Del Pozzo[bj,ae], R. De Pietri[bh,ac], R. De Rosa[bf,aa], C. De Rossi[ao,k], T. Dietrich[ar], L. Di Fiore[aa], C. Di Giorgio[bq,ai], F. Di Giovanni[by], M. Di Giovanni[bw,aj], T. Di Girolamo[bf,aa], A. Di Lieto[bj,ae], S. Di Pace[bm,af], I. Di Palma[bm,af], F. Di Renzo[bj,ae], M. Drago[n,y], J.-G. Ducoin[al], O. Durante[bq,ai], M. Eisenmann[am], L. Errico[bf,aa], D. Estevez[am], V. Fafone[bn,ag,n], S. Farinon[x], F. Feng[b], I. Ferrante[bj,ae], F. Fidecaro[bj,ae], I. Fiori[k], D. Fiorucci[n,y], R. Fittipaldi[h,ai], V. Fiumara[bk,ai], R. Flaminio[am,ap], J.A. Font[by,as], J.-D. Fournier[c], S. Frasca[bm,af], F. Frasconi[ae], V. Frey[al], G. Fronzé[ak], L. Gammaitoni[bi], F. Garufi[bf,aa], G. Gemme[x], E. Genin[k], A. Gennai[ae], Archisman Ghosh[ar], B. Giacomazzo[bw,aj], J.M. Gonzalez Castro[bj,ae], M. Gosselin[k,bj,ae], R. Gouaty[am], A. Grado[u,aa], M. Granata[ao], G. Greco[bx,w], A. Grimaldi[bw,aj], S.J. Grimm[n,y], P. Groot[at], P. Gruning[al], G.M. Guidi[bx,w], Y. Guo[ar], P. Gupta[ar], O. Halim[y,n], T. Harder[c], J. Harms[n,y], A. Heidmann[an], H. Heitmann[c], P. Hello[al], G. Hemming[k], T. Hinderer[m,ar,j], D. Hofman[ao], D. Huet[al], V. Hui[am], B. Idzkowski[d], A. Iess[bn,ag], G. Intini[bm,af], J.-M. Isac[an], T. Jacqmin[an], P. Jaranowski[ax], R.J.G. Jonker[ar], S. Katsanevas[k], F. Kéfélian[c], I. Khan[n,ag], N. Khetan[n,y], G. Koekoek[ar,bd], S. Koley[ar], A. Królak[aq,r], A. Kutynia[aq], D. Laghi[bj,ae], A. Lartaux-Vollard[al], C. Lazzaro[ab], P. Leaci[bm,af], N. Leroy[al], N. Letendre[am], F. Linde[o,ar], M. Llorens-Monteagudo[by], A. Longo[bo,ah], M. Lorenzini[n,y], V. Loriette[l], G. Losurdo[ae], D. Lumaca[bn,ag], A. Macquet[c], E. Majorana[af], I. Maksimovic[l], N. Man[c], V. Mangano[bm,af], M. Mantovani[k], M. Mapelli[bg,ab], F. Marchesoni[ay,ad], F. Marion[am], A. Marquina[bz], S. Marsat[b], F. Martelli[bx,w], V. Martinez[q], A. Masserot[am], S. Mastrogiovanni[b], J. Meidam[ar],

** Corresponding author.
* Corresponding author.
E-mail addresses: diego.bersanetti@ge.infn.it (D. Bersanetti), julia.casanueva@pi.infn.it (J. Casanueva Diaz).

https://doi.org/10.1016/j.astropartphys.2019.07.005

E. Mejuto Villa[bt,ai], L. Mereni[ao], M. Merzougui[c], F. Messina[be,z], R. Metzdorff[an], A. Miani[bw,aj], C. Michel[ao], L. Milano[bf,aa], A. Miller[bm,af], O. Minazzoli[c,i], Y. Minenkov[ag], M. Montani[bx,w], F. Morawski[e], B. Mours[am], F. Muciaccia[bm,af], A. Nagar[g,ak,p], I. Nardecchia[bn,ag], L. Naticchioni[bm,af], J. Neilson[bt,ai], G. Nelemans[at,ar], C. Nguyen[b], D. Nichols[m,ar], S. Nissanke[m,ar], F. Nocera[k], M. Obergaulinger[by,av], G. Oganesyan[n,y], G. Pagano[bj,ae], G. Pagliaroli[n,y], C. Palomba[af], P.T.H. Pang[ar], F. Pannarale[bm,af], F. Paoletti[ae], A. Paoli[k], D. Pascucci[ar], A. Pasqualetti[k], R. Passaquieti[bj,ae], D. Passuello[ae], M. Patil[r], B. Patricelli[bj,ae], R. Pedurand[ao,bc], A. Perego[bw,aj], C. Périgois[am], A. Perreca[bw,aj], O.J. Piccinni[bm,af], M. Pichot[c], F. Piergiovanni[bx,w], V. Pierro[bt,ai], G. Pillant[k], L. Pinard[ao], I.M. Pinto[bt,ai,g], W. Plastino[bo,ah], R. Poggiani[bj,ae], P. Popolizio[k], E.K. Porter[b], G.A. Prodi[bw,aj], M. Punturo[ad], P. Puppo[af], G. Raaijmakers[m,ar], N. Radulescu[c], P. Rapagnani[bm,af], M. Razzano[bj,ae], T. Regimbau[am], L. Rei[x], P. Rettegno[ak,bv], F. Ricci[bm,af], G. Riemenschneider[bv,ak], F. Robinet[al], A. Rocchi[ag], L. Rolland[am], M. Romanelli[bl], R. Romano[bp,aa], D. Rosińska[d], P. Ruggi[k], O.S. Salafia[t,be,z], L. Salconi[k], A. Samajdar[ar], N. Sanchis-Gual[f], E. Santos[c], B. Sassolas[ao], O. Sauter[am], P. Schmidt[at], D. Sentenac[k], V. Sequino[x], A. Sharma[n,y], M. Sieniawska[e], N. Singh[d], A. Singhal[n,af], F. Sorrentino[x], M. Spera[bg,ab], C. Stachie[c], D.A. Steer[b], G. Stratta[s,w], A. Sur[e], B.L. Swinkels[ar], M. Tacca[ar], S. Tiwari[bw,aj], M. Tonelli[bj,ae], A. Torres-Forné[a], F. Travasso[k,ad], M.C. Tringali[d], A. Trovato[b], L. Trozzo[bu,ae], K.W. Tsang[ar], M. Valentini[bw,aj], N. van Bakel[ar], M. van Beuzekom[ar], J.F.J. van den Brand[aw,ar], C. Van Den Broeck[ar,ba], L. van der Schaaf[ar], M. Vardaro[bg,ab], M. Vasúth[au], G. Vedovato[ab], D. Verkindt[am], F. Vetrano[bx,w], A. Viceré[bx,w], J.-Y. Vinet[c], H. Vocca[bi,ad], R. Walet[ar], M. Was[am], A.R. Williamson[m,ar], A. Zadrożny[aq], T. Zelenova[k], J.-P. Zendri[ab]

[a] *Max Planck Institute for Gravitationalphysik (Albert Einstein Institute), D-14476 Potsdam-Golm, Germany*
[b] *APC, AstroParticule et Cosmologie, Université Paris Diderot, CNRS/IN2P3, CEA/Irfu, Observatoire de Paris, Sorbonne Paris Cité, Paris Cedex 13 F-75205, France*
[c] *Artemis, Université Côte d'Azur, Observatoire Côte d'Azur, CNRS, CS 34229, Nice Cedex 4 F-06304, France*
[d] *Astronomical Observatory Warsaw University, Warsaw 00–478, Poland*
[e] *Nicolaus Copernicus Astronomical Center, Polish Academy of Sciences, Warsaw, 00–716, Poland*
[f] *Centro de Astrofí sica e Gravitação (CENTRA), Departamento de Fí sica, Instituto Superior Técnico, Universidade de Lisboa, Lisboa 1049-001, Portugal*
[g] *Museo Storico della Fisica e Centro Studi e Ricerche "Enrico Fermi", I-00184 Roma, Italyrico Fermi, Roma I-00184, Italy*
[h] *CNR-SPIN, c/o Università di Salerno, Fisciano, Salerno, I-84084, Italy*
[i] *Centre Scientifique de Monaco, 8 quai Antoine Ier, MC-98000, Monaco*
[j] *Delta Institute for Theoretical Physics, Science Park 904, GL Amsterdam 1090, The Netherlands*
[k] *European Gravitational Observatory (EGO), Cascina,Pisa, I-56021, Italy*
[l] *ESPCI, CNRS, Paris F-75005, France*
[m] *GRAPPA, Anton Pannekoek Institute for Astronomy and Institute of High-Energy Physics, University of Amsterdam, Science Park 904, Amsterdam 1098 XH, The Netherlands*
[n] *Gran Sasso Science Institute (GSSI), L'Aquila I-67100, Italy*
[o] *Institute for High-Energy Physics, University of Amsterdam, Science Park 904, Amsterdam 1098 XH, The Netherlands*
[p] *Institut des Hautes Etudes Scientifiques, F-91440 Bures-sur-Yvette, France*
[q] *Université de Lyon, Université Claude Bernard Lyon 1, CNRS, Institut Lumière Matière, F-69622 Villeurbanne, France*
[r] *Institute of Mathematics, Polish Academy of Sciences, Warsaw 00656, Poland*
[s] *INAF, Osservatorio di Astrofisica e Scienza dello Spazio, Bologna I-40129, Italy*
[t] *INAF, Osservatorio Astronomico di Brera sede di Merate, Merate, Lecco,I-23807, Italy*
[u] *INAF, Osservatorio Astronomico di Capodimonte, Napoli I-80131, Italy*
[v] *INAF, Osservatorio Astronomico di Padova, Padova I-35122, Italy*
[w] *INFN, Sezione di Firenze, Sesto Fiorentino, Firenze, I-50019, Italy*
[x] *INFN, Sezione di Genova, Genova I-16146, Italy*
[y] *INFN, Laboratori Nazionali del Gran Sasso, Assergi I-67100, Italy*
[z] *INFN, Sezione di Milano-Bicocca, Milano I-20126, Italy*
[aa] *INFN, Sezione di Napoli, Complesso Universitario di Monte S.Angelo, Napoli I-80126, Italy*
[ab] *INFN, Sezione di Padova, Padova I-35131, Italy*
[ac] *INFN, Sezione di Milano Bicocca, Gruppo Collegato di Parma, Parma I-43124, Italy*
[ad] *INFN, Sezione di Perugia, Perugia I-06123, Italy*
[ae] *INFN, Sezione di Pisa, Pisa I-56127, Italy*
[af] *INFN, Sezione di Roma, Roma I-00185, Italy*
[ag] *INFN, Sezione di Roma Tor Vergata, Roma I-00133, Italy*
[ah] *INFN, Sezione di Roma Tre, Roma I-00146, Italy*
[ai] *INFN, Sezione di Napoli, Gruppo Collegato di Salerno, Complesso Universitario di Monte S. Angelo, Napoli I-80126, Italy*
[aj] *INFN, Trento Institute for Fundamental Physics and Applications, Trento, I-38123 Povo, Italy*
[ak] *INFN Sezione di Torino, Torino I-10125, Italy*
[al] *LAL, Univ. Paris-Sud, CNRS/IN2P3, Université Paris-Saclay, Orsay F-91898, France*
[am] *Laboratoire d'Annecy de Physique des Particules (LAPP), Univ. Grenoble Alpes, Université Savoie Mont Blanc, CNRS/IN2P3, F-74941 Annecy, France*
[an] *Laboratoire Kastler Brossel, Sorbonne Université, CNRS, ENS-Université PSL, Collège de France, Paris F-75005, France*
[ao] *Laboratoire des Matériaux Avancés (LMA), CNRS/IN2P3, Villeurbanne F-69622, France*
[ap] *National Astronomical Observatory of Japan, 2-21-1 Osawa, Mitaka, Tokyo 181–8588, Japan*
[aq] *NCBJ, 05–400 Świerk-Otwock, Poland*
[ar] *Nikhef, Science Park 105, Amsterdam 1098 XG, The Netherlands*

[as] Observatori Astronòmic, Universitat de València, València E-46980, Paterna, Spain
[at] Department of Astrophysics/IMAPP, Radboud University Nijmegen, P.O. Box 9010, Nijmegen 6500 GL, The Netherlands
[au] Wigner RCP, RMKI, H-1121 Budapest, Konkoly Thege Miklós út 29–33, Hungary
[av] Institut für Kernphysik, Theoriezentrum, Darmstadt 64289, Germany
[aw] VU University Amsterdam, 1081 HV Amsterdam, The Netherlands
[ax] University of Białystok, Białystok 15–424, Poland
[ay] Università di Camerino, Dipartimento di Fisica, Camerino, I-62032, Italy
[az] Dipartimento di Fisica, Università degli Studi di Genova, Genova I-16146, Italy
[ba] Van Swinderen Institute for Particle Physics and Gravity, University of Groningen, Nijenborgh 4, Groningen 9747 AG, The Netherlands
[bb] Theoretisch-Physikalisches Institut, Friedrich-Schiller-Universität Jena, Jena D-07743, Germany
[bc] Université de Lyon, Lyon F-69361, France
[bd] Maastricht University, P.O. Box 616, 6200 MD Maastricht, The Netherlands
[be] Università degli Studi di Milano-Bicocca, Milano I-20126, Italy
[bf] Università di Napoli 'Federico II,' Complesso Universitario di Monte S.Angelo, Napoli I-80126, Italy
[bg] Università di Padova, Dipartimento di Fisica e Astronomia, Padova I-35131, Italy
[bh] Dipartimento di Scienze Matematiche, Fisiche e Informatiche, Università di Parma, Parma I-43124, Italy
[bi] Università di Perugia, Perugia I-06123, Italy
[bj] Università di Pisa, Pisa I-56127, Italy
[bk] Scuola di Ingegneria, Università della Basilicata, Potenza I-85100, Italy
[bl] Univ Rennes, CNRS, Institut FOTON - UMR6082, Rennes F-3500, France
[bm] Università di Roma 'La Sapienza', Roma I-00185, Italy
[bn] Università di Roma Tor Vergata, Roma I-00133, Italy
[bo] Dipartimento di Matematica e Fisica, Università degli Studi Roma Tre, Roma I-00146, Italy
[bp] Dipartimento di Farmacia, Università di Salerno, Salerno, I-84084 Fisciano, Italy
[bq] Dipartimento di Fisica "E.R. Caianiello," Università di Salerno, Salerno, I-84084 Fisciano, Italy
[br] Dipartimento di Ingegneria Industriale (DIIN), Università di Salerno, Salerno, I-84084 Fisciano, Italy
[bs] Dipartimento di Medicina, Chirurgia e Odontoiatria "Scuola Medica Salernitana," Università di Salerno, Salerno, I-84081 Baronissi, Italy
[bt] Dipartimento di Ingegneria, Università del Sannio, Benevento I-82100, Italy
[bu] Università di Siena, Siena I-53100, Italy
[bv] Dipartimento di Fisica, Università degli Studi di Torino, Torino I-10125, Italy
[bw] Università di Trento, Dipartimento di Fisica, Trento, I-38123 Povo, Italy
[bx] Università degli Studi di Urbino "Carlo Bo," Urbino I-61029, Italy
[by] Departamento de Astronomía y Astrofísica, Universitat de València, E-46100 Burjassot, València, Spain
[bz] Departamento de Matemáticas,Universitat de València, E-46100 Burjassot, València, Spain

ARTICLE INFO

Article history:
Received 11 April 2019
Revised 25 July 2019
Accepted 29 July 2019
Available online 10 September 2019

Keywords:
Gravitational wave detectors
Interferometer
Suspended optical cavities
Control loops

ABSTRACT

Following a successful period of data-taking between 2006 and 2011, the Virgo gravitational-wave detector was taken offline for a major upgrade. The changes made to the instrument significantly increased the complexity of the control systems and meant that an extended period of commissioning was required to reach a sensitivity appropriate for science data-taking. This commissioning period was completed in July of 2017 and the second-generation Advanced Virgo detector went on to join the Advanced LIGO detectors in the O2 science run in August of the same year. The upgraded detector was approximately twice as sensitive to binary neutron star mergers as the first-generation instrument. During the August 2017 science run, Advanced Virgo detected its first gravitational wave signal, with the binary black hole merger, GW170729. This paper describes the control of the longitudinal degrees of freedom in the Advanced Virgo instrument during the O2 science run and the process that brought the detector from an uncontrolled, non-resonant state to its target working point.

1. Introduction

General Relativity predicted the existence of gravitational waves (GWs) in 1916. GWs are perturbations of the metric, caused by an acceleration of non-rotationally symmetric mass, which propagate at the speed of light. As their interaction with matter is very weak, they provide information that is not accessible via the electro-magnetic (EM) spectrum, opening a new observational window on the universe. Compact objects, such as binary black holes and neutron stars, as well as other cataclysmic events, such as supernova explosions, are the sources that emit the most powerful GWs, i.e. those with amplitudes, upon reaching the Earth, of $h \sim 10^{-23}$ $Hz^{1/2}$. The study of GWs will improve our understanding of these astrophysical events and make it possible to test General Relativity.

Since the first prediction of the existence of GWs, a great deal of time and effort have been spent on attempting to detect them [1]. Interferometric antennas, which are sensitive to differential displacements, such as those produced during the passage of a GW, proved to be the most promising detectors. The first generation of ground-based interferometers, composed of two four-kilometre-long detectors in the United States (LIGO), one three-kilometre-long detector in Italy (Virgo) and one detector 600 m long in Germany (GEO600), concluded a period of joint data-taking, which spanned three separate runs, in 2011. Despite the fact that an actual detection was not made, relevant astrophysical results were still achieved [2,3]. The data-taking runs also served to test the working principle of the interferometers, as well as to prove their robustness. Furthermore, significant instrument developments were made possible as a result of the experience gained during the first generation.

A clear path from the first- to the second-generation antennas was established. The Advanced LIGO and Advanced Virgo detectors aimed to increase their sensitivity by a factor of ten with respect to the first generation. To this end, a series of major upgrades were implemented that required an intense period of commissioning. The Advanced LIGO detectors made the first detection of a GW on the 14th of September, 2015, the merger of a binary black hole (BBH) [4], proving that it was possible to make astrophysical observations using ground-based interferometric detectors.

Advanced Virgo began taking scientific data alongside the Advanced LIGO interferometers on the 1st of August, 2017, during the run known as 'O2' (Observational Run 2). The inclusion of Virgo in this run, which was to conclude on the 25th of the same month, contributed to improving the localisation and parameter estimation of the detected sources: two BBH and, for the first time, a binary neutron star (BNS) [5]. The role of Advanced Virgo was especially relevant in the latter case, as it made it possible to improve the sky localisation enough to allow for a more efficient electro-magnetic follow-up.

The Advanced Virgo detector was intensively commissioned during the year prior to its joining the O2 scientific run. In this article, the main challenges encountered during this period are presented, with particular focus on the longitudinal control strategy used to bring the Advanced Virgo detector to its target working point and to keep it there in a reliable and robust way. Both the modelling and the experimental results are presented.

2. Working principle of the detector

Interferometric GW detectors are based on the principle of the Michelson interferometer. Differential laser path length changes in the two arms of the interferometer are detected as a change in the laser interference pattern at the detector. The passage of a GW perturbs the metric which produces such a differential change and moves the interferometer away from the working point. Thus the GW is measured as a change of light power on the detection photodiode. For this reason, the performance of these detectors is fundamentally limited by shot noise. Moreover, in order to decouple intensity noise from the measurement, the optimal working point is destructive interference, also known as the dark fringe condition.

The shot noise limited sensitivity of Michelson interferometer is related to the length of the two arms and the input laser power. In practice, even with arm lengths of 3-km, the basic Michelson configuration is unable to achieve the required sensitivity to measure GWs, which have amplitudes of $h \sim 10^{-23}$ $Hz^{-1/2}$. Two upgrades were necessary in order to reach the target sensitivity. First, the effective arm lengths were increased by converting each arm into 3-kilometre long Fabry-Perot cavity; thereby increasing the optical path traversed by the laser beam, amplifying the signal. Second, the effective input power was increased by adding a power-recycling mirror (PR) between the laser source and the beam splitter mirror (BS). The power reflected back to the laser source at dark fringe is recycled back into the interferometer increasing the effective power of the input beam, thus increasing the signal-to-noise ratio (SNR) and the sensitivity [6]. Fig. 1 shows the Advanced Virgo optical scheme.

2.1. Longitudinal degrees of freedom

The working point of the interferometer can be described by four longitudinal degrees of freedom (DoF):

- MICH: the difference in the lengths of the short arms of the MICHelson: $l_N - l_W$;
- PRCL: the Power-Recycling Cavity Length: $l_{PR} - \frac{l_N+l_W}{2}$;
- DARM: the Differential lengths of the ARM cavities (this is the degree of freedom that is sensitive to the passage of GWs: $L_N - L_W$);
- CARM: the average (Common) length of the ARM cavities (this degree of freedom is particular, in that it is sensitive not only to mirror motion, but also to the frequency noise of the laser: $\frac{L_N+L_W}{2}$).

The Fabry-Perot and power-recycling cavities (CARM, DARM and PRCL) need to be kept on resonance to maximise the optical path travelled by the light inside the inferometer. In addition, the

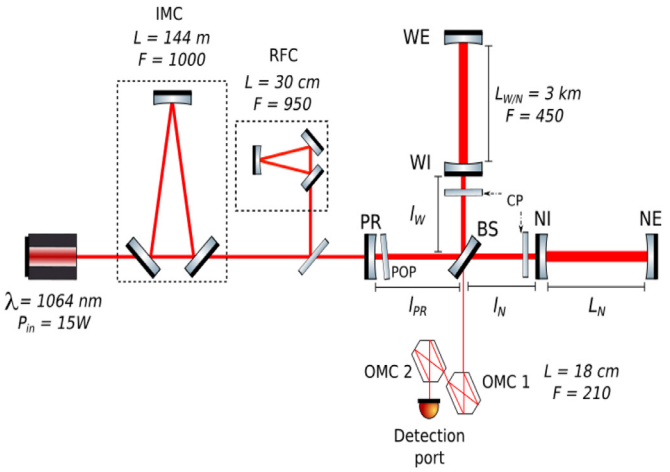

Fig. 1. Optical scheme of the Advanced Virgo interferometer: IMC is the Input Mode Cleaner, RFC is the Reference Cavity, PR is the Power Recycling mirror, POP is the Pick-Off Plate, BS is the Beam Splitter mirror, CPs are the Compensation Plates, WE and WI are the West End and Input mirrors respectively, NE and NI are the North End and Input mirrors respectively and OMC 1 and 2 are the two Output Mode Cleaners. The most relevant lengths (L) and finesses (F) are shown.

Michelson is brought to the dark fringe and the working point is thus achieved.

Seismic noise produces a residual oscillatory motion of the mirrors on the order of 1 μm rms, despite the attenuation provided by elaborate suspension systems [7], the so-called 'Superattenuators'. The working point of all of the DoF is rarely crossed simultaneously while the mirrors are free-swinging. Therefore, in order to bring interferometer to its working point and keep it there, a very precise active control of the position of the mirrors is needed. Giving just one example: the total rms for DARM is required to be $\lesssim 10^{-16}$ m not only to remain at the working point but also to not worsen the sensitivity. For the latter it is necessary to take in account the DARM working point, as well as the presence of high signal-to-noise lines, which can produce upconversion of low frequency noise [8].

3. Longitudinal control

The longitudinal control, known as the 'lock', uses negative feedback control loops acting on mirror positions to set the correct lengths of the longitudinal degrees of freedom or, in another words, to set the correct phase of the laser beam travelling through the different degrees of freedom. For this purpose, real-time information of by how much these phases are far from the working point is needed. The error signals carrying this information are generated by using a variant of the Pound-Drever-Hall (PDH) technique [9]. Sidebands are generated around the carrier laser beam frequency by using radio frequency phase modulation of the input carrier beam with an electro-optic modulator (EOM). The frequency of this sidebands is chosen to be anti-resonant on the arm cavities while the carrier is resonant, so that they can act as a phase reference. The phase difference between the carrier, which enters the cavity, and the sidebands, which are rejected by it and thus constant, provides the requested information. The beat note between the carrier and the sidebands is extracted by demodulating photodiode signals at the modulation frequency (f_m).

In order to control the four degrees of freedom, the frequency of the sidebands need to be chosen carefully:

- f_{m1} (6.270777 MHz) is used to control the arm cavities. For this purpose it needs to be resonant inside the power-recycling cavity, in order to be able to reach the arm cavities, and it needs to be anti-resonant in the arm cavities;

Table 1
Bandwidth of the longitudinal controls in Advanced Virgo during O2.

DOF	Bandwidth
DARM	70 Hz
MICH	18 Hz
CARM	10 kHz
PRCL	40 Hz

- f_{m2} (8.361036 MHz) is used to control the power-recycling cavity, so it needs to be anti-resonant within it.

Demodulated photodiode signals are generated at several optical points of the interferometer which allows error signals with the highest SNR and lowest cross-coupling to be chosen for each DOF. The photodiode signals are acquired via analogue-to-digital converters (ADC) and are sent to a series of real-time computers, which run at 10 kHz, where they are processed.

The demodulation and filtering of the error signals, which are undertaken in order to calculate the needed corrections, are done digitally by these real-time computers. The digital demodulation is innovative with respect to the other gravitational-wave detectors and allows greater flexibility in the lock-acquisition system [10]. These corrections are then sent to the digital signal processors (DSP) of the suspensions, running at 40 kHz, which re-filter them and calculate the amount of current that is needed to be applied to the actuators: four pairs of coil-magnets per mirror.

The bandwidth of the control loops is mainly limited to approximately 100 Hz by the delay introduced in the digital chain. This is sufficient to allow to reach the accuracy requirements of the longitudinal control, see Table 1. However, this is not the case for the frequency noise, which is relevant across a much larger bandwidth (up to several hundreds of kHz). Due to this, the control of CARM is not implemented using the real-time computers but via a special DSP, which runs at 500 kHz and which makes it possible to obtain a control bandwidth of about 10 kHz. This bandwidth is higher than the response of the coil-magnet actuator used for the mirrors in the other longitudinal control loops which begins to decrease in the region of a few Hz. Instead, the laser itself is used.

4. Advanced Virgo control challenges

The first generation of gravitational-wave detectors [11] provided a better understanding of the limiting noises. These can be divided into two main groups: *fundamental*, such as shot noise and thermal noise, and *technical*, such as diffused light, phase noise and control noises [12,13]. In order to decrease these noise sources for Advanced Virgo, a series of major upgrades were undertaken, which are described in detail in [14]. This paper presents those upgrades that had the most significant impact on the control of the interferometer:

1. **Marginally-stable power-recycling cavity:** in order to reduce as much as possible the effect of mirror-coating thermal noise on the arm cavities, the radius of curvature of the mirrors that form the end points of each arm cavity, was chosen to ensure that the beam size is maximal upon them. As a consequence of this change of geometry and considering the limited space available in the area surrounding the mirror, the curvature of the power-recycling mirror was also changed. This pushed the power-recycling cavity (PRC) stability conditions very close to the instability limit.
   In this context, the stability refers to the quality of the superposition of the spatial eigenmodes of the beam resonating inside an optical cavity [15]. An optical cavity is unstable when it does not have a Gaussian beam that can resonate inside it. The g-factor of a cavity is a parameter that characterises its stability and which depends only on geometrical considerations; in this case the length of the cavity and radius of curvature of the mirrors. A cavity is considered stable when its g-factor is between 0 and 1. The g-factor of the Advanced Virgo PRC is very close to 1 and thus to the upper limit: $1 - g = 0.19 \cdot 10^{-5}$. Consider that, for Virgo+ - an earlier Virgo configuration - this g-factor was $1 - g = 4 \cdot 10^{-5}$, and so provided a stability margin that was twenty times greater.
   Such a marginal stability has a strong impact on the distribution of the Higher Order Modes (HOMs), the separation of which ($\sim$11 kHz) is much smaller than the cavity line-width ($\sim$210 kHz). As a result, the cavity is very close to being degenerate; meaning, that the resonance condition for the HOMs is met almost at the resonance for the fundamental mode. The generation of HOMs translates into a loss of power on the main mode (both for the carrier and the sidebands), decreasing the signal-to-noise ratio (SNR) of the error signals. Furthermore, for almost degenerate cavities, the HOMs resonate with the fundamental mode, further degrading the quality of the error signals by adding offsets, multiple zero-crossings or distorting the linear region. The creation of HOMs occurs in the presence of misalignment, mismatch and optical aberrations in general, which means that the control of the interferometer is extremely sensitive to them. For example, a typical misalignment of $\sim$0.5 µm leads to a loss of optical gain of the error signals, due to the formation of HOMs of about 80% [16], which is too high to ensure the stability of the longitudinal controls.
   To avoid instabilities in the controls, the requirements in terms of the angular accuracy of the mirrors became too stringent, particularly during the transients of the lock acqusition. For this reason, it was necessary to look for a solution to deal with the optical-gain fluctuations. The sidebands were the most affected, as these are not cleaned of HOMs by the arm cavities, as opposed to the carrier (they are resonant only in the PRC).
   The goal was to make the sidebands insensitive to HOMs. The so called Schnupp asymmetry played a key role in attempts to achieve this objective [6]. In order to be able to build an error signal at the dark port, while being at the dark fringe (carrier in destructive interference), it is necessary that the sidebands also reach the dark port as well. Since the interference condition depends on the frequency, a macroscopic length difference between the short Michelson arms can be added so that the carrier is in destructive interference, but not the sidebands. This offset is called Schnupp asymmetry.
   Due to the Schnupp asymmetry, the higher the modulation frequency, the more power leaks towards the detection port. This implies major losses inside the PRC and thus a lower finesse. A cavity with a low finesse has the advantage of being less sensitive to HOMs, since it already has high losses and so any extra loss does not have a significant impact. So with a higher modulation frequency it is possible to control the PRC in a robust way [17], in spite of its marginally-stable nature.
   This was confirmed using simulations. In particular the optical-gain loss of the error signals in the presence of a misalignment for different modulation frequencies was studied [18]. The chosen frequency, 56.436993 MHz ($9f_{m1}$), was a multiple of the nominal frequency, in order to ensure that the resonance conditions were the same. For this frequency the PRC has a finesse of 13, while for the 6 MHz the finesse is 77.

Thanks to this high-modulation frequency it was possible to lock the interferometer on the dark fringe in a stable way. However, due to the marginally-stable nature of the PRC, it was necessary to adapt the whole lock-acquistion sequence, including the alignment.

2. **Increased finesse of the arm cavities:** for Advanced Virgo the finesse of the arm cavities was increased to 450 (a factor of three greater than the Virgo+ finesse) in order to increase the power circulating inside the arms and thus improve the sensitivity at high frequencies.
   Having such a high finesse makes the cavities more sensitive to dynamical effects, which makes acquiring the lock even more difficult. As the cavity mirrors are moving, when the beam impinges upon them a Doppler effect takes place, shifting the beam frequency. This effect accumulates with each round-trip and when the total frequency shift is of the order of the cavity line-width, the electric fields start to become distorted, which leads to an effect also known as *ringing* [19].
   In particular, the critical velocity above which these effects start to appear in Advanced Virgo is 0.35 μm/s, which is below the residual velocity of the arm cavities. A strategy has been adopted to overcome this problem, based on the Guided Lock technique. The details of this control acquisition strategy are given in [20].
3. **Increased radiation pressure in the arm cavities:** as a consequence of the change of the geometry of the arm cavities, the mirror angular DOFs can not be actuated in a single mirror basis, but require a mixed driving. Moreover, the increase of the arm cavities finesse and of the input power (up to 15 W), implies that radiation pressure has a stronger impact. For these reasons the angular control of the arm cavities is more complicated in Advanced Virgo.
4. **New topology of the frequency stabilisation:** The demodulation of photodiode output for use as error signals, as well as the controller for the frequency stabilisation are done digitally for Advanced Virgo [10]; whereas they were done analogically in Virgo and Virgo+. This allows for more flexibility in the selection of the demodulation frequency (f, 2f, 3f) increasing the information available to describe the behaviour of the interferometer, without the need of hardware changes. Moreover, it also allows more freedom to design the controller and to adapt it to the commissioning needs. The major impact on the frequency stabilisation was regarding its topology.
   The second stage of frequency stabilisation (SSFS) is a complex loop, since it uses a single error signal for two different actuators: a mirror (up to 200 Hz) and the laser frequency (up to 10 kHz). This implies that the global stability depends not only on each of the branches but also in how they interact. In the past, the system was analogic so the simplest topology for designing the controls was to feed the correction of the fast branch into the slow loop [21]. This implied that both controls needed to be engaged at the same time, increasing the difficulty of commissioning the system. With the digital system though, there are less constraints for the control design, so the error signal is simply sent to both branches. This way it is possible to engage the slow and fast loops one after the other, simplifying the commissioning process. So overall, the digital demodulation implementation added more flexibility to the frequency stabilisation, however it implied a major effort in terms of initial commissioning of this new technology.
5. **Gravitational-wave readout:** the detection technique has been changed from heterodyne (RF), which is highly dependent on the sideband quality, to homodyne (DC readout) [12,13]. This implies adding a microscopic differential offset so that there is a static carrier field that reaches the detection port, in order to work slightly off of the dark fringe. In this way, the DC power can be used as an error signal, since its slope is different from zero (see Fig. 2), and a differential motion caused by a gravitational wave will translate into a power variation. In Advanced Virgo, the offset is added to the DARM DoF, which means that the arm cavities work slightly off-resonance. In particular, the offset was chosen as a compromise between the photodiode saturation level and the DARM optical gain, which means having ∼9 mW reaching the detection port.

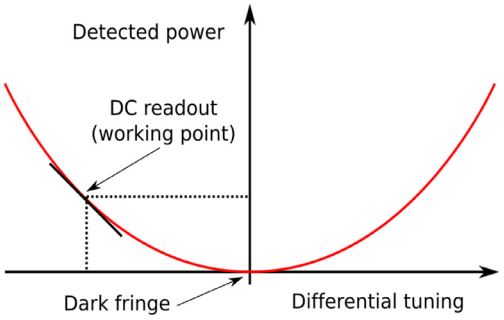

Fig. 2. Variation of the power at the detection port as a function of a differential offset in the arms.

4.1. Lock-acquisition sequence: variable finesse

As mentioned previously, it is unlikely that the four degrees of freedom cross their working point simultaneously, while the actuators do not have enough dynamics to stop all of the mirrors at the same time. For this reason a sequential control strategy is necessary. For Virgo and Virgo+ the *variable finesse* strategy was developed [23]. In order to ease the process, it first removes one degree of freedom (PRCL) by considerably misaligning the power-recycling mirror. This reduces the coupling between the remaining DoF and makes it possible to engage their control independently of one another.

Secondly, the Michelson is controlled in an intermediate interference condition, or *half-fringe*. The whole interferometer can then be considered a composed Fabry-Perot cavity, in which the input mirror is responsible for the power-recycling and the end mirror is an effective mirror, the reflectivity of which depends on the arm cavities and the Michelson. So when MICH is in half-fringe, the losses of this compound mirror increase, lowering the finesse of the effective power-recycling cavity. This intermediate state makes it easier to acquire the control of the power-recycling cavity, because of the low finesse. At this point, the Michelson is slowly brought to the dark fringe, passing through a series of stable, intermediate states along the way. This strategy was used for Virgo and Virgo+, but it was necessary to adapt it to the new optical configuration of Advanced Virgo. The new strategy is described in detail in this section, which focusses on the applied changes.

In practice, the control acquisition starts by misaligning the PR mirror by 60 μrad on the horizontal plane. This misalignment is enough to make the PRC disappear. The first step is to engage the **control of the arm cavities** using a variation of the Guided Lock strategy, as mentioned above. The error signals used are obtained by demodulating the power transmitted by the arm cavities at 6 MHz, normalised by the transmitted power. By misaligning the power-recycling mirror, the two cavities become completely independent, which makes it possible to engage the control of each of the cavities simultaneously.

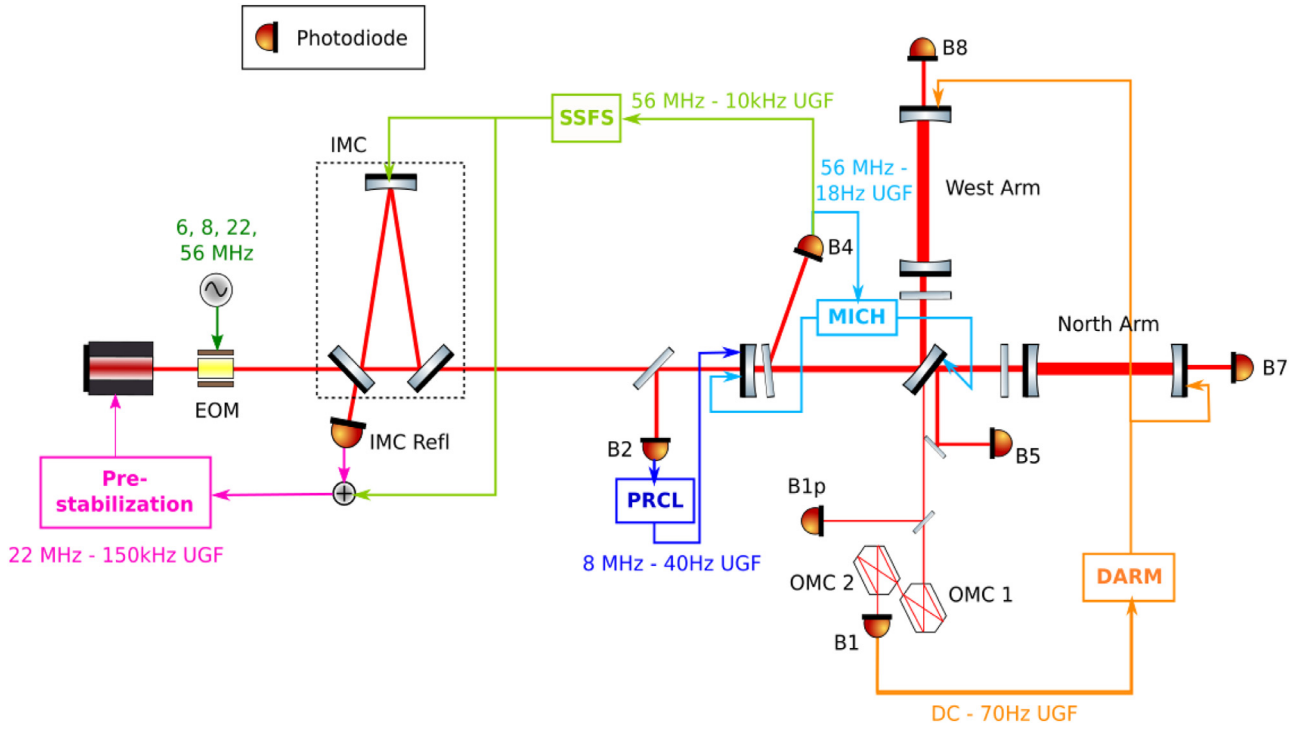

Fig. 3. Scheme of the interferometer showing all of the photodetectors available and those which are used to control the longitudinal degrees of freedom.

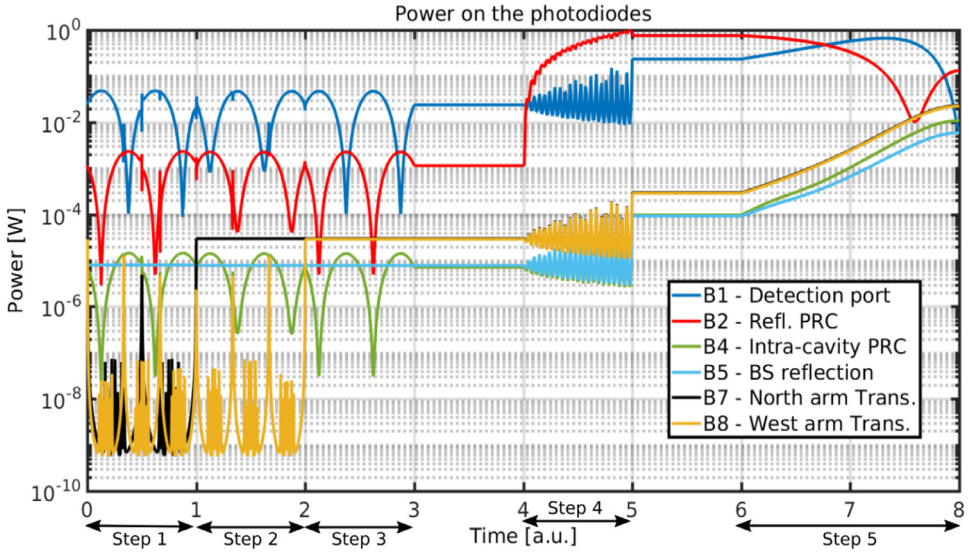

Fig. 4. Simulation made using the Finesse simulation package [22] of the power evolution during the lock acquisition in the different monitoring points of the interferometer, with 1W of input power. Step 1 corresponds to the lock of the north arm, Step 2 to the lock of the west arm, Step 3 to the lock of the Michelson in half-fringe, Step 4 to the alignment of the PR and, finally, Step 5 corresponds to the decrease of the MICH offset in the lead up to the reaching of the dark fringe.

Once the arm cavities are on resonance, the **control of the Michelson DoF** is engaged at half-fringe. Since this working-point is far from the nominal one, the error signal is built using a DC signal, which comes, in the main, from the detection port, prior to the output mode cleaners (OMCs) (B1p), as shown in Fig. 3. In order to simplify the fringe definition, the error signal is normalised using the total power recombining at the beam splitter (B1p + αB4), with α being the calibration factor between the maximum power reaching B1p and B4 photodiodes. This allows to have an error signal that carries direct information about the interference condition; that is, it has a value of 1 in bright fringe and of 0 in dark fringe. To engage the control of MICH in half-fringe it is enough to add an offset to the error signal of 0.5.

At this point, the control of the arm cavities is transformed to the two longitudinal DoF, **CARM** and **DARM** (the period between Steps 3 and 4 in Fig. 4). This is merely a change of basis and, as such, is transparent for the performance of the interferometer, since the error signals in use do not change. However, it makes it possible to engage the **Second Stage of Frequency Stabilisation** (SSFS), the control of the CARM DoF with a higher bandwidth, by acting upon the laser frequency instead. The transition is made at this stage because the arm cavities provide a better reference than the Input Mode Cleaner (IMC, see Fig. 1), which is used for the first stage of stabilisation, since their linewidth frequency is lower (100 Hz for the arms with respect to 1000 Hz for the IMC). The error signal used is B4, demodulated at

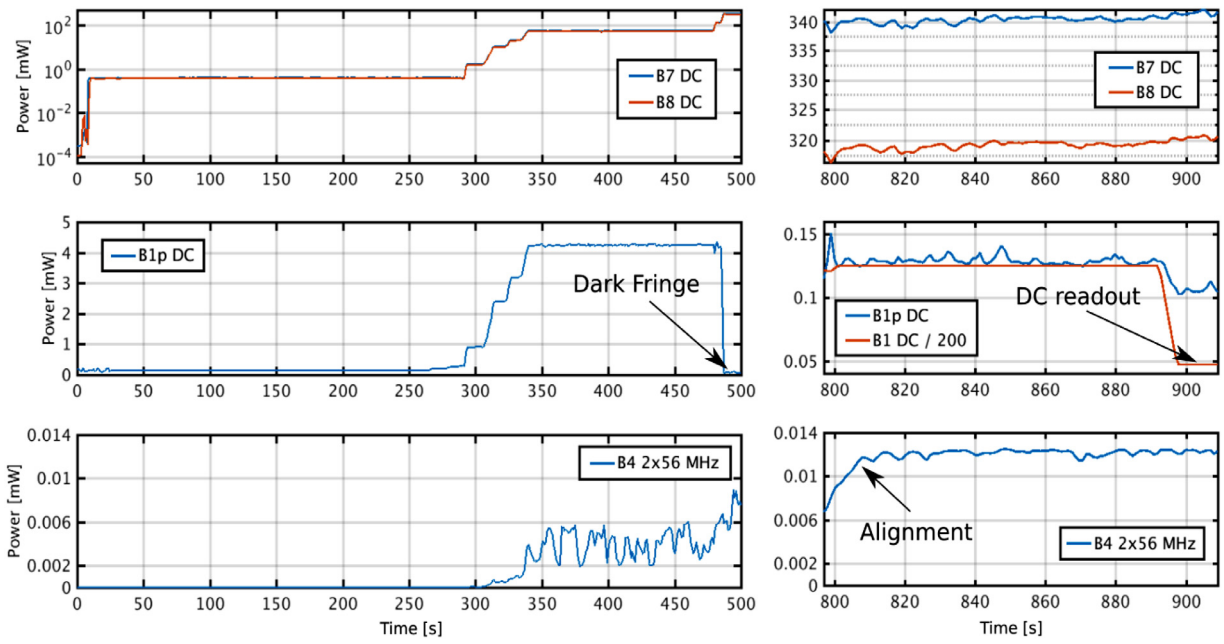

Fig. 5. Power evolution during the lock acquisition. The upper plots show the power transmitted by the end cavities. B7 shows the North-Arm cavity, B8 shows the West. The central plots show the power reaching the detection photodiode (B1p). The bottom plots show the power carried by the 56 MHz sideband, monitored inside the power-recycling cavity (B4).

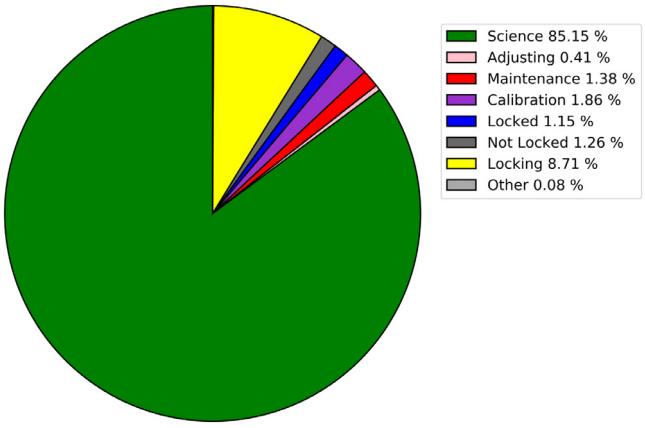

Fig. 6. Pie chart of the time spent by the interferometer in the different configurations during the Virgo O2 data taking.

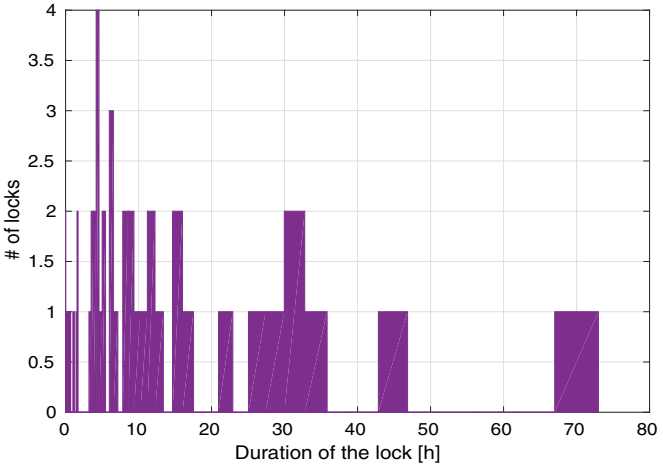

Fig. 7. Duration of the locks during the O2 scientific run.

56 MHz, which monitors the power reflected by the arm cavities towards the laser.

As mentioned previously, the digital demodulation makes it possible to undertake this passage in two steps. First, the new error signal is filtered and the correction is used to control the length of the IMC, with a bandwidth of 200 Hz. This is equivalent to changing the laser frequency because the analogue loop, which locks the frequency of the laser to the IMC length up to 300 kHz (pre-stabilisation) is active. In a second step, the error signal is filtered and sent directly to the laser, which allows actuation at higher frequencies, particularly up to 10 kHz.

The PR mirror is then aligned, and the PRCL loop is engaged as soon as the build up of the cavity is high enough to do so (more than 50%). The error signal used for this DoF is the reflection of the PRC (B2) demodulated at 8 MHz, which is the sideband that is reflected by the PRC. This step is critical, since the power increases significantly in all of the photodetectors, as is shown in Step 4 of Fig. 4, changing the optical gain of all of the error signals. Moreover, during the aligning process, there are extra gain fluctuations due to the crossing of several resonances of the carrier and sidebands. These fluctuations correspond to the peaks shown in Fig. 4. For this reason it is important to normalise them using the power circulating inside the interferometer, in order to reduce these optical-gain fluctuations. At this stage, a first angular control of the PR mirror is engaged. This is key in order to avoid large gain fluctuations and to reduce the presence of HOMs inside the interferometer.

Finally, with the four longitudinal degrees of freedom under control, the reduction of the MICH offset begins. This produces non-negligible changes in the power being recycled in the interferometer, since the reflectivity of the effective end mirror starts to increase, as can be seen in Step 5 of Fig. 4. In particular, the minimum on the reflected power (red curve on Fig. 4) shows the moment at which the reflectivity of the effective end mirror is such that the cavity is critically coupled, and as the MICH offset keeps decreasing, it becomes over coupled. The normalisation of the error signals also contributes to maintaining the stability of the controls during this stage.

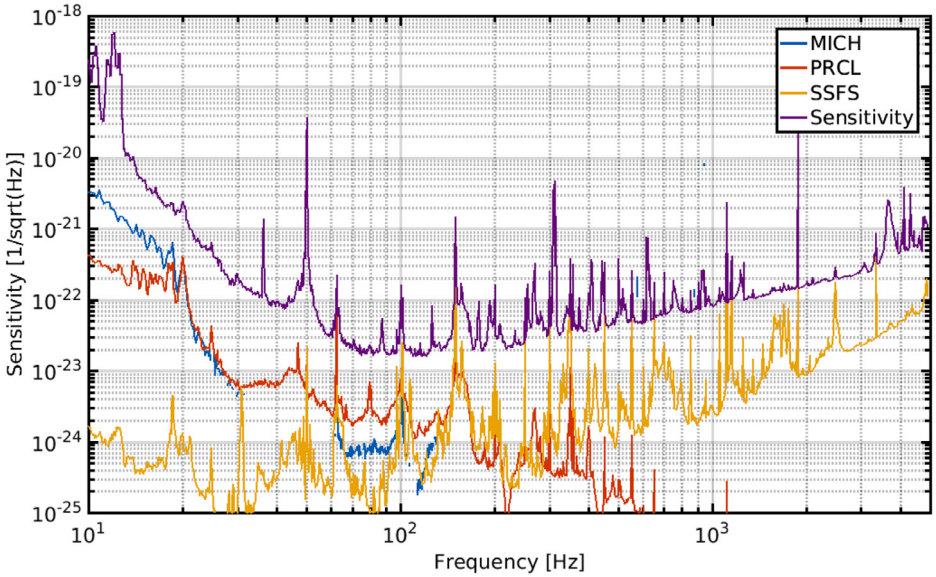

Fig. 8. Contribution of the longitudinal controls to the sensitivity. The purple line is the sensitivity during O2. The colored lines represent the contribution of the longitudinal degrees of freedom to the sensitivity: MICH (blue), PRCL (red) and SSFS (yellow). This shows that the sensitivity is not limited by the longitudinal controls.

When the MICH offset is 0.1, the transition to the dark fringe takes place. However, the region around the dark fringe; that is, the minimum of the parabola (see Fig. 2), is a critical point, because the optical gain decreases down to 0. For this reason, the transition is done over a period lasting one second, during which time the MICH offset is put to zero and the error signal is simultaneously handed-off to an RF signal, the quadrature of B4 demodulated at 56 MHz.

After reaching the dark fringe, the DARM error signal is replaced by B1p, demodulated at 56 MHz. Prior to this point, the error signal is built using B7 and B8 demodulated at 6 MHz, although the signal-to-noise ratio is very low, because the anti-resonant condition of the sidebands in the arms makes it difficult for them to reach the photodiodes in transmission. The whole control sequence up to this point takes approximately five minutes, as is shown in Fig. 5. At this stage, to further improve the robustness, the control of the angular degrees of freedom is engaged. The stabilising effect is clear from the behaviour of the sidebands, as shown in Fig. 5.

The last step in the lock-acquisition strategy is the switch to DC readout. The two OMCs play a key role in this stage, since they clean any spurious field that might degrade the SNR. The transition towards the final DARM error signal is made in two steps: once the first OMC is locked, its transmission is used, which becomes a good error signal following the addition of an offset to DARM. Then, after the lock of the second OMC, the DARM offset is tuned so that 9 mW reach the B1 photodiode. B1 becomes the new and final error signal (see Fig. 5).

The interferometer is then at its working point, and so the target becomes not only the robustness, but also the sensitivity. For this purpose, a longitudinal-noise substraction is engaged in order to reduce the coupling of the MICH degree of freedom to DARM, improving the sensitivity [24] [25].

5. Conclusion: performance in O2

On the 1st of August, 2017, Advanced Virgo joined the O2 run, taking data for almost a month alongside the Advanced LIGO detectors, with a duty cycle of 85%, as shown in Fig. 6. The performance of the controls made it possible to keep the interferometer at its working point for a maximum time during a single lock of 69 and a half hours. The typical durations of the locks are shown in Fig. 7, showing a mean duration of $\sim$10h.

Regarding the lock-acquisition sequence, the average time taken to transition from a free-moving interferometer to reaching the working point, was 14 minutes. This is limited by the time to lock the OMCs, since it is necessary to scan their working point using a thermal actuator, which has a long thermal constant. To reduce this duration, the lock of the OMCs can be optimized and the number of cavities can be reduced to one.

Fig. 8 shows an example of a sensitivity curve during O2, including the contributions of the remaining degrees of freedom [26]. The control noises are below the sensitivity curve and therefore do not limit the performance of the detector. The typical online sensitivity of Advanced Virgo during O2 was 27 Mpc, measured in terms of the maximum distance at which a standard binary neutron star merger can be detected. This led to the first triple detection of a gravitational wave, coming from a binary black hole [27], and the first detection ever of a binary neutron star inspiral [5].

In order to improve the sensitivity several upgrades are foreseen for the next scientific runs, which will increase further the complexity of the lock acquisition. In order to improve the sensitivity at high frequency, where it is shot-limited, the input power will be increased. This will increase the thermal effects inside the ITF as well as the radiation pressure. Also, a new optical cavity will be installed, the Signal Recycling Cavity. This will improve the sensitivity, but it will add a new DoF to be controlled, and thus a new control strategy.

References

[1] J. Weber, Gravitational radiation, Phys. Rev. Lett. 18 (1967) 498–501 doi:10.1103/PhysRevLett.18.498.
[2] B. Abbott, et al., Beating the spin-down limit on gravitational wave emission from the crab pulsar, Astrophys. J. 683 (2011).
[3] B. Abbott, et al., Beating the spin-down limit on gravitational wave emission from the vela pulsar, Astrophys. J. 737 (2011).
[4] B. Abbott, et al., Observation of gravitational waves from a binary black hole merger, Phys. Rev. Lett. 116 (2016).
[5] B. Abbott, et al., Gw170817: Observation of gravitational waves from a binary neutron star inspiral, Phys. Rev. Lett. 119 (2017).
[6] P. Saulson, Fundamentals of Interferometric Gravitational Wave Detectors, World Scientific, 1994.
[7] F. Acernese, et al., Measurements of superattenuator seismic isolation by virgo interferometer, Astropart. Phys. 33 (2010).

[8] G. Vajente, Advanced Virgo length sensing and control steady state design, Technical note, Virgo, 2011. http://www.tds.virgo-gw.eu/ql/?c=8797.
[9] R.W.P. Drever, J.L. Hall, F.V. Kowalski, J. Hough, G.M. Ford, A.J. Munley, H. Ward, Laser phase and frequency stabilization using an optical resonator, Appl. Phys. B 31 (1983).
[10] T. Bouedo, et al., Tests of the digital demodulation prototype board for the AdV photodiode readout, Technical note, Virgo, 2012. http://www.tds.virgo-gw.eu/ql/?c=9299.
[11] T. Accadia, et al., Performance of the virgo interferometer longitudinal control system during the second science run, Astropart. Phys. 34 (2011) 521–527.
[12] S. Hild, et al., DC-readout of a signal-recycled gravitational wave detector, Class. Quantum Gravity 26 (5) (2009).
[13] T. T. Fricke, et al., DC readout experiment in enhanced Ligo, Classi. Quantum Gravity 29 (2011).
[14] F. Acernese, et al., The Advanced Virgo detector, Journal of physics: conference series 610 (2015), (pages 012014).
[15] A. Siegman, Lasers, University Science Books, 1986.
[16] A. Allocca, A. Chiummo, M. Mantovani, Locking strategy for the advanced Virgo central iunterferometer, Technical note, Virgo, 2016. http://www.tds.virgo-gw.eu/ql/?c=11495.
[17] G. Vajente, R. Day, J. Marque, AdV optical layout: new parameters proposal, Presentation IR-0377B-11, Virgo, 2011. http://www.tds.virgo-gw.eu/ql/?c=8432.
[18] J. Casanueva, M. Mantovani, Central Interferometer simulations: study of different locking strategies, Technical note, Virgo, 2016. http://www.tds.virgo-gw.eu/ql/?c=11684.
[19] M.J. Lawrence, B.W. et al., Dynamic response of a fabryperot interferometer, J. Opt. Soc. Am. B 16 (4) (1999).
[20] A. Allocca, D. Bersanetti, J. Casanueva Diaz, H. Heitmann, D. Hoak, M. Mantovani, B. Swinkels, New algorithm for the guided lock technique for a high-finesse optical cavity (2019), Manuscript under journal review.
[21] F. Bondu, Some issues with a multiple servo loop system, Technical note, Virgo, 2004. http://www.tds.virgo-gw.eu/ql/?c=1434.
[22] A. Freise, et al., Frequency domain interferometer simulation with higher-order spatial modes, Class. Quant. Grav. 21 (5) (2004).
[23] F. Acernese, et al., The variable finesse locking technique, Class. Quantum Gravity 23 (2006) S85–S89.
[24] F. Acernese, et al., Performance of the virgo interferometer longitudinal control system during the second science run, Astropart. Phys. 33 (2010).
[25] B. Swinkels, E. Campagna, G. Vajente, L. Barsotti, M. Evans, Longitudinal noise subtraction: the alpha-, beta- and gamma-technique, Technical note, Virgo, 2016. http://www.tds.virgo-gw.eu/ql/?c=2055.
[26] M. W. for LIGOV. collaborations, Advanced Virgo and LIGO: today and tomorrow, Presentation at a conference, 24th Congres General de la Societe Francaise de Physique, 2017.
[27] B. Abbott, et al., Gw170814: a three-detector observation of gravitational waves from a binary black hole coalescence, Phys. Rev. Lett. 119 (2017).